Chemical Engineering Journal 402 (2020) 126144

Contents lists available at ScienceDirect

Chemical Engineering Journal

journal homepage: www.elsevier.com/locate/cej

Electronic coupling strategy to boost water oxidation efficiency based on the modelling of trimetallic hydroxides $Ni_{1\text{-}x\text{-}y}Fe_xCr_y(OH)_2$: From theory to experiment

Jun Ma[a,b], Pengsong Li[a], Xiao Lin[c], Yijun Huang[a], Yang Zhong[a], Lipeng Zhang[a], Xiaoming Sun[a], Daojin Zhou[a,*], Wen-Feng Lin[b,*], Zhenhai Xia[d,*]

[a] State Key Laboratory of Chemical Resource Engineering, Beijing Advanced Innovation Center for Soft Matter Science and Engineering, College of Chemical Engineering & College of Chemistry, Beijing University of Chemical Technology, Beijing 100029, China
[b] Department of Chemical Engineering, Loughborough University, Loughborough, Leicestershire LE11 3TU, UK
[c] Department of Chemical Engineering and Biotechnology, University of Cambridge, Cambridge CB3 0AS, UK
[d] Department of Materials Science and Engineering, University of North Texas, Denton 76203, USA

HIGHLIGHTS

- Structure-reactivity relation of $Ni_{1\text{-}x}Fe_x(OH)_2$ was elucidated at electronic level.
- Chromium substitution was predicted as a promoter for OER by computational data.
- $Ni_{1\text{-}x\text{-}y}Fe_xCr_y(OH)_2$ with superior activity was synthesized based on DFT prediction.
- Electronic coupling strategy provides a principle for screening efficient catalyst.

GRAPHICAL ABSTRACT

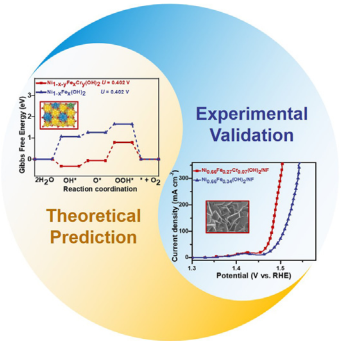

ARTICLE INFO

Keywords:
Electronic coupling
Oxygen evolution reaction
Ternary hydroxide
DFT simulations
Experimental validation

ABSTRACT

Developing low-cost yet highly efficient earth-abundant electrocatalysts for oxygen evolution reaction (OER) is of great significance for industrial scale water splitting for clean hydrogen production, as well as for rechargeable metal-air batteries. In searching for advanced catalysts, it is equally important to fundamentally understand working mechanism and be able to rationally design and manipulate catalytic sites. Starting from the density functional theory (DFT) calculations as a guidance, our theoretical model revealed that chromium substitution in nickel–iron hydroxides ($Ni_{1\text{-}x}Fe_x(OH)_2$) not only accelerated the charge transfer but also regulated the adsorption energy of OER intermediates to achieve optimal binding strength. Experimentally, chromium was doped into the laminate of $Ni_{1\text{-}x}Fe_x(OH)_2$, resulting in the enhanced catalytic performance for oxygen evolution reaction, which confirmed the predictions from the theoretical data. The porous and ultra-thin ternary $Ni_{1\text{-}x\text{-}y}Fe_xCr_y(OH)_2$ electrocatalysts were grown directly on a nickel foam (NF) substrate, with an optimum composition $Ni_{0.66}Fe_{0.27}Cr_{0.07}(OH)_2$/NF identified, which exhibited a superior OER performance, i.e., achieving a significant current density of 10 mA cm^{-2} at a low overpotential of 231 mV, a small Tafel slope (31 mV dec^{-1}) and an excellent stability at a highly oxidative potential of 1.68 V vs RHE in alkaline electrolyte. The comprehensive study involving both theoretical and experimental results in this work provides an insightful guidance in designing efficient OER catalysts for chemical and electrical energy conversion and storage.

---

[*] Corresponding authors.
E-mail addresses: zhoudj@mail.buct.edu.cn (D. Zhou), W.Lin@lboro.ac.uk (W.-F. Lin), zhenhai.xia@unt.edu (Z. Xia).

https://doi.org/10.1016/j.cej.2020.126144
Received 12 April 2020; Received in revised form 13 June 2020; Accepted 28 June 2020

1. Introduction

Hydrogen is one of the most promising clean energy carriers to replace fossil fuels and solve the environmental pollution problem for the 21st century [1,2]. Alternatively, water splitting via electrocatalytic technology serves as a potential way to produce clean and sustainable hydrogen in industrial scale [3,4]. As an important electrochemical half-reaction of water splitting, the oxygen evolution reaction (OER) at anode is a kinetically sluggish process, which requires overcoming a significant activation barrier to accelerate four electrons transfer [5,6]. In recent years, although noble metal-based catalysts (such as IrO_2 and RuO_2) have shown great OER performances [7], they are not suitable for large-scale industrial applications mainly due to their high prices and rare reserves on the earth. Therefore, it is very desirable to design and develop low cost yet highly efficient electrocatalysts for the OER.

Two-dimensional transition metal-based hydroxides (2D-TMHs) have been widely recognized as an asset for reinforcing water oxidation performance on account of their tunable layered structure and controllable dispersion of high valent metallic cations [8,9,10]. Among various 2D-TMHs catalysts, nickel–iron 2D-TMHs, of which the formal composition is $[Ni^{II}_{1-x}Fe^{III}_{x}(OH)_2]^{x+}$ $[x/nA^{n-}]\cdot zH_2O$, where A = anions, as the benchmark, has exhibited outstanding OER activity with a low overpotential and high electrolysis current density in alkaline solution [11,12]. In principle, it has been demonstrated that the intrinsic activity of the nickel–iron 2D-TMHs could be further enhanced multiply by modifying them with the other heteroatoms, such as manganese (Mn) [13,14], cobalt (Co) [15,16], and vanadium (V) [17]. As a cheap and earth-abundant transition metal, Cr was supposed to be a versatile promoter in electronic structures. On the one hand, Cr^{3+}, with the roughly equivalent radius to Fe^{3+}, was facile to access the matrix but not perturb the original framework. On the other, the Cr with a lower electronegativity than that of Fe, was endowed a role of electro-donating to induce the charge redistribution of the active sites flexibly. More importantly, introducing Cr into the lattice of the oxides and hydroxides has been evolving into an attractive priority to enhance the OER activity by courtesy of more indispensable reasons than that of the other transition metals (such as Mn, Co and V) in recent years. Firstly, Cr-based oxides/(oxy)hydroxides possesses favorable excellent electrical conductivity, such as $LaCrO_3$ and CrOOH [18,19]. Secondly, the Cr in 3d-group presents the multi-electron orbitals ($3d^5 4s^1$). A series of multi-oxidation states (+1, +2, +3, +4, +5 and + 6) make it easily being oxidized to higher oxidation states [20], which in return exert a positive influence on the active Fe sites during preparation and reaction [21]. Thirdly, a unique type of electronic configuration ($t^3_{2g}e^0_g$) of Cr^{3+} cation is suitable for electron capture and charge transfer, which is likely to play a synergistic modulator between redox-active cations [22,23]. Last but not the least, among a diverse set of the materials library, high-throughput screening and material-genome engineering directly identified that a mixed component comprising of Ni-Fe-Cr was essential for water oxidation, which deserved more attention for the sake of further investigation in catalytic mechanism [24,25]. Based on these irreplaceable aspects, incorporating Cr into transition-metal based catalyst was recognized as a practicable route to achieve high-efficiency in the electrocatalysis for OER [26]. For example, via electrochemical measurements, Wang and co-workers demonstrated that the outstanding performance of ternary amorphous metal oxide was derived from the containing of Cr [27]. Jin's group also reported that Cr-containing oxides/(oxy)hydroxides exhibited a remarkable intrinsic OER catalytic activity. Nevertheless, it is not yet clear that how the guest element interplays with the host materials, and how the local electronic environments are activated by accommodating foreign composition [28]. In addition, in the previous reports, there have been seldom attempts to analyze and predict the catalytic activity according to the correlation between the electronic characteristics and working mechanism before synthesis. Trial-and-error approaches are still commonly utilized to date for the screen and preparation of highly efficient catalysts.

To rationally design a catalyst, it is critical to understand the structure–reactivity relationship at the atomic and electronic levels [29]. The insights gained from the catalytic mechanism studies can guide the experiments to create active sites for highly efficient catalysts [30,31]. With this in mind, the density functional theory with Hubbard *U* (DFT + *U*) [32,33], a quantum mechanics tool, was employed to better investigate the model catalyst of multi-electron systems, of which chromium (Cr)-doped $Ni_{1-x}Fe_x(OH)_2$ being selected preferentially as a representative. Cr substitution was envisioned to be an appropriate choice to facilitate water oxidation, attributing to the electronic coupling.

Inspired by the above analysis, herein, we present a theoretically and experimentally combined study to illustrate the significant role of electronic coupling effect on a model catalyst of Cr doped $Ni_{1-x-y}Fe_xCr_y(OH)_2$ for OER. Based on computational prediction, a facile approach was applied to in-situ construct the ternary $Ni_{1-x-y}Fe_xCr_y(OH)_2$ nanosheets array on a nickel foam (NF) substrate, which significantly outperformed the benchmark $Ni_{1-x}Fe_x(OH)_2$ catalyst for oxygen evolution reaction as predicted. This study may serve as a promising strategy in the rational design and preparation of efficient OER catalysts.

2. Computational and experimental details

2.1. Theoretical models and methods

The plane wave Vienna ab-Initio Simulation Package (VASP) code was put to utilize for the construction and calculation of all modeling catalysts originated in the first-principle [34]. The complicated correlation effects from electron and core in interior of $Ni_{1-x}Fe_x(OH)_2$ and $Ni_{1-x-y}Fe_xCr_y(OH)_2$ was expressed by projector augmented wave (PAW) pseudo-potentials method and the Generalized Gradient Approximation (GGA)-Perdew-Burke-Ernzerh (PBE) with turning on spin polarization [35,36]. Simultaneously, aiming to increase the accuracy of the strongly correlated systems, we amended the on-site coulomb and exchange interactions for 3d-group elements according to the Hubbard-*U* approach put forward by Dudarev et al [37]. According to the previous studies, based on the traditional DFT method, the *U-J* values of 3.40, 3.29 and 2.79 were implemented to 3d-transition metals of Ni, Fe and Cr [38,39,40,41]. The two types of K-point sampling were generated by Monkhorst-Pack Scheme to optimize periodic structure (3 × 3 × 1) and analyze electronic structure (5 × 5 × 1), both of which were selected with the cut-off energy 400 eV. The typical reciprocal points of G (0,0,0), Z (0,0,1/2), F (0,1/2,0) and Q (1/2,0,0) were selected for EB from the previous study [21]. The calculation did not terminate until the accuracy was reached, with the energy and the force converged less than 1×10^{-4} eV and 0.05 eV/Å, respectively.

The OER follows the four-electron transfer process:

$$OH^- + * \rightarrow *OH + e^- \tag{1}$$

$$OH^- + *OH \rightarrow *O + H_2O(l) + e^- \tag{2}$$

$$OH^- + *O \rightarrow *OOH + e^- \tag{3}$$

$$OH^- + *OOH \rightarrow O_2(g) + * + H_2O(l) + e^- \tag{4}$$

Where *, *OH, *O, and *OOH represents the active sites and the intermediates (OH, O, OOH) adsorbed at the active sites, and $\triangle G_1$, $\triangle G_2$, $\triangle G_3$ and $\triangle G_4$ stand for the Gibbs free energy of elementary steps (1–4), calculated by the computational standard hydrogen electrode (SHE) model.

The free energy calculation is listed as follows:

$$\Delta G_1 = 1/2E(H_2) + E(*OH) - E(*) - E(H_2O) + \Delta ZPE - T\Delta S - eU + K_bT\ln 10\cdot pH$$

$$\Delta G_2 = 1/2E(H_2) + E(*O) - E(*OH) + \Delta ZPE - T\Delta S - eU + K_bT\ln 10\cdot pH$$

$$\Delta G_3 = 1/2E(H_2) + E(*OOH) - E(H_2O) - E(*O) + \Delta ZPE - T\Delta S - eU + K_bT\ln 10\cdot pH$$

$$\Delta G_4 = 4.92 - \Delta G_3 - \Delta G_2 - \Delta G_1$$

Among the ΔG_1, ΔG_2, ΔG_3 and ΔG_4, the maximum one was recorded as ΔG_{max}, and the overpotential is defined in equation:
$\eta = \Delta G_{max}/e - 1.23$ V.

2.2. Chemicals and materials

Urea, ethanol, nickel nitrate *hexa*-hydrate, ferric nitrate nine-hydrate and chromium nitrate *hexa*-hydrate, KOH (99%), HCl (~37%) and Nickel foam (NF) were purchased from Aladdin Company. Deionized pure water was used for preparation of solution.

2.3. Preparation of $Ni_{1-x-y}Fe_xCr_y(OH)_2$/NF, $Ni_{1-x}Fe_x(OH)_2$/NF $Ni_{1-x}Cr_x(OH)_2$/NF and RuO_2/NF electrodes

In a hydrothermal method, the double hydroxide nanosheet arrays were synthesized in one-step. Firstly, nickel, iron and chromium precursors with the total amount of mole at 1.0 mmol while having different ratios of 1:0:0, 0.66:0.34:0, 0.66:0.27:0.07, 0.66:0.17:0.17, 0.66:0.07:0.27 and 0.66:0:0.34, were ultrasonically dissolved in pure water for 10 min. In the meanwhile, NF was carefully cleaned before use, it was immersed in the solutions followed the order of HCl, ethanol and pure water, in an ultrasonic bath to eliminate impurities. The solution containing reactants (36 mL) and NF with exposed nickel atoms were transferred to the polytetrafluoroethylene lining. The reaction was sustained for 12 h in the stainless-steel autoclave at 120 °C. It was rinsed with ethanol and water for several times before being put to dry in vacuum oven at 60 °C for 8 h.

Synthesis of RuO_2/NF electrode: 5 mg RuO_2, 1 mg carbon powder and 10 μL Nafion solution were dispersed in 1 mL ethanol by sonication for 30 mins. Then 0.5 mL of the RuO_2 ink was loaded onto a 1 cm^2 NF.

2.4. Characterization

The images of morphology were captured by field-emission

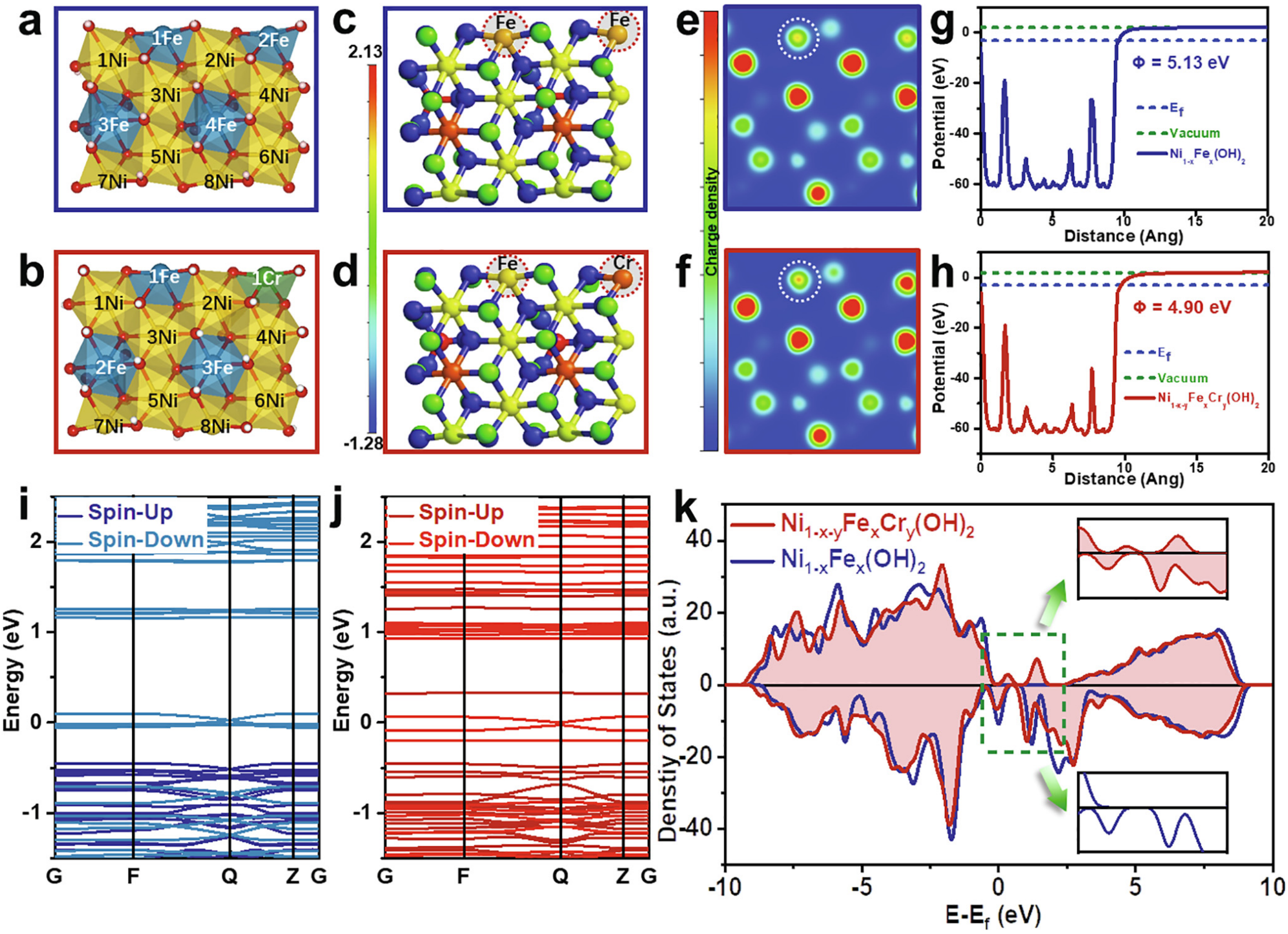

Fig. 1. The main results obtained from the DFT + *U* calculations of $Ni_{1-x-y}Fe_xCr_y(OH)_2$ (in red) and $Ni_{1-x}Fe_x(OH)_2$ (in blue); (a-b) the model shown in (a) is the optimized structure of $Ni_{1-x}Fe_x(OH)_2$ and that shown in (b) is for $Ni_{1-x-y}Fe_xCr_y(OH)_2$, the yellow, blue, green, white, red and brown are behalf of Ni, Fe, Cr, O, H and C atoms, respectively; (c-d) the Bader charge distributions for $Ni_{1-x}Fe_x(OH)_2$ (c) and $Ni_{1-x-y}Fe_xCr_y(OH)_2$ (d); (e-f) the electron density evolution of pristine $Ni_{1-x}Fe_x(OH)_2$ (e) and $Ni_{1-x-y}Fe_xCr_y(OH)_2$ (f); (g-h) electrostatic potentials of the $Ni_{1-x}Fe_x(OH)_2$ (g) and $Ni_{1-x-y}Fe_xCr_y(OH)_2$ (h) by work functions; (i-j) the band structures for the $Ni_{1-x}Fe_x(OH)_2$ (i) and $Ni_{1-x-y}Fe_xCr_y(OH)_2$ (j); (k) the TDOS curve of $Ni_{1-x-y}Fe_xCr_y(OH)_2$ and $Ni_{1-x}Fe_x(OH)_2$, where the narrower bandgap unveils a more conductive structure. The upper right and lower right corners are zoomed in on the green dotted line. (For interpretation of the references to colour in this figure legend, the reader is referred to the web version of this article.)

scanning electron microscope (SEM, JEOL JEM-6335) with energy dispersive X-ray spectroscopy (EDS) and High-resolution transmission electron microscopy (HRTEM, JEOL JEM-2100, at 200 kV). X-ray powder diffraction (XRD, Rigaku D/max 2500) using Cu Kα was carried out (step size = $10^{\circ}\ min^{-1}$ from 10 to 80). X-ray photoelectron spectroscopy (XPS) was performed on an ESCALAB 250. The band gap was calculated from the UV–visible diffuse reflectance spectra measured by UV-2600.

2.5. Electrochemical measurements

The Chenhua electrochemical workstation (CH Instruments 660E) was adopted to the performance measurement in a three-electrode cell with O_2-saturated 1.0 M KOH (sparged for at least 30 min before and during data collection) at 298 K. The counter electrode and reference electrode were a platinum foil and a saturated calomel electrode (SCE), respectively. The nickel foam (NF) without and with in-situ grown catalysts (NF, $Ni_{0.66}Fe_{0.27}Cr_{0.07}(OH)_2$/NF, $Ni_{0.66}Fe_{0.34}(OH)_2$/NF, $Ni_{0.66}Cr_{0.34}(OH)_2$/NF) were used as the working electrode directly, which have an area of 1 cm^2. All potentials cited were iR calibrated and converted to reversible hydrogen electrode (RHE) scale by the equation: $E_{RHE} = E_{SCE} + 0.241 + 0.059 \cdot pH$. The turnover frequency (TOF) for the four electrons involved in the OER process was obtained by the equation: $TOF = j \times s/(4F \times n)$, where j, s, F and n represent the current density (A cm^{-2}) at a given overpotential, the surface area of the electrode, the Faraday constant (96480C mol^{-1}) and the amount of catalyst in moles (mol cm^{-2}).

3. Results and discussion

Theoretical models of octahedral $Ni_{1-x}Fe_x(OH)_2$ as shown in Fig. 1(a) and $Ni_{1-x-y}Fe_xCr_y(OH)_2$ in Fig. 1(b) were conducted firstly, based on the density functional theory (DFT) + U simulation, as previous experimental reports. All cations were in a highly monodisperse state rather than a randomly distribution in the nanosheets. Firstly, the formation energy was computed via the equation: $E_f = E_{doped} + \mu_{Fe} - (E_{\text{un-doped}} + \mu_{Cr})$, where E_{doped} and $E_{\text{un-doped}}$ were the total energy of the supercell with $Ni_{1-x-y}Fe_xCr_y(OH)_2$ and $Ni_{1-x}Fe_x(OH)_2$, respectively. The μ_{Fe} and μ_{Cr} are the chemical potential of one heteroatom in the most stable crystal phase. According to this definition, the negative value of E_f (-0.72 eV) for this most possible model elucidated its high thermodynamic stability (Table S1-S2) and the possibility of being synthesized practically. Secondly, the electronic structures of 2D-TMHs were evaluated, which were closely related to their OER performances as shown in Fig. 1(c-k). In order to express the charge distribution more intuitively, the shades of colour were utilized to reflect it (Fig. 1c-d). Except for the circled parts (active Fe site and Cr-doping site), in the elsewhere the changes in colour were almost indistinguishable. Consistent with that, the changing values of the Bader charges at all Ni sites were imperceptible and almost negligible, when compared $Ni_{1-x}Fe_x(OH)_2$ with $Ni_{1-x-y}Fe_xCr_y(OH)_2$ (Table S4). It manifested that rarely interplaying between Ni and Cr came into being. Hence, the electron flow from Cr to Fe through Fe-O-Cr bonds was confirmed by the Bader charge of Fe, which decreased from + 1.50 to + 1.37 once Cr was introduced into $Ni_{1-x}Fe_x(OH)_2$ lattice. The electron-rich state of Fe can

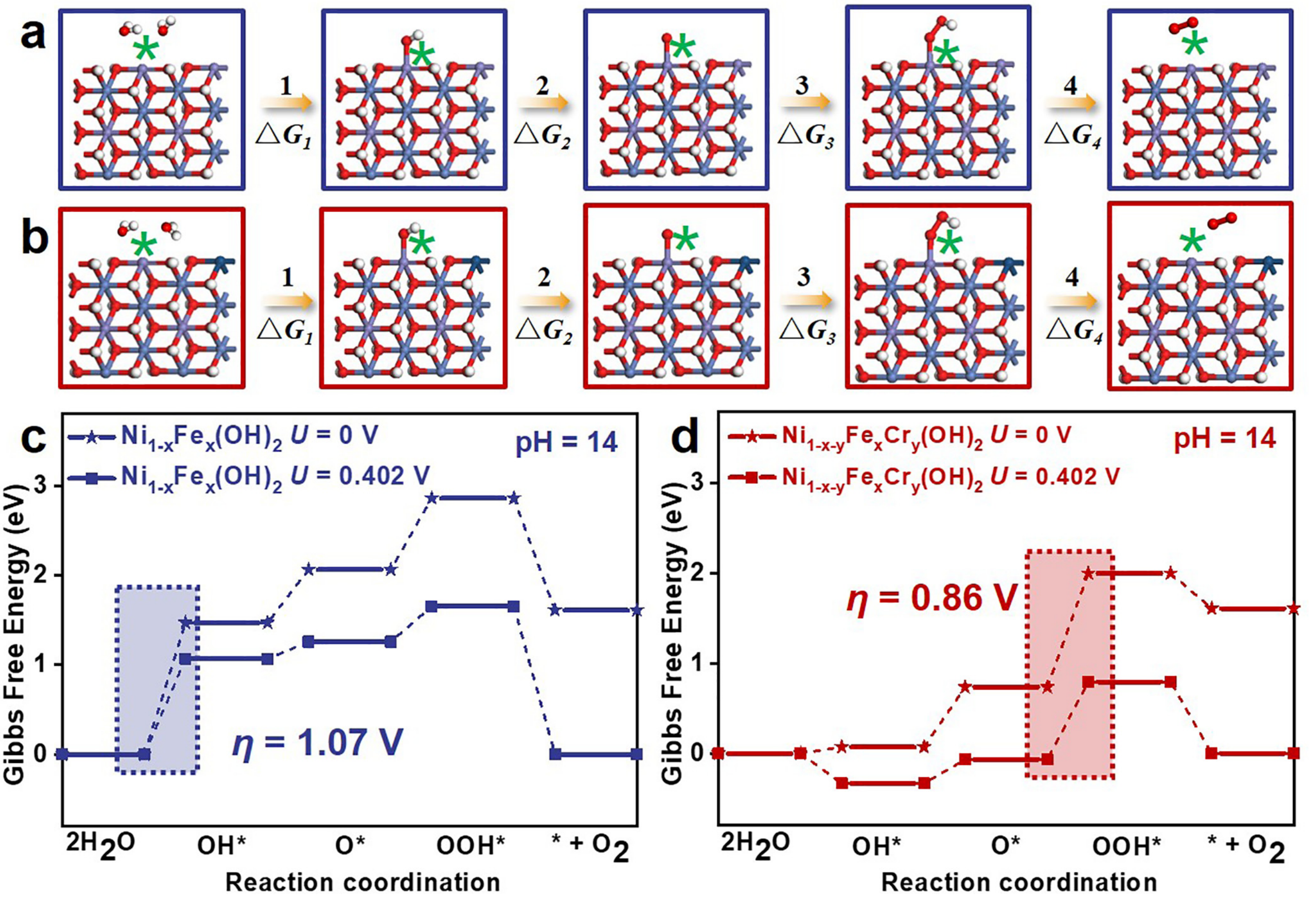

Fig. 2. The main results for the oxygen evolution reaction (OER) processes on $Ni_{1-x}Fe_x(OH)_2$ (a) and $Ni_{1-x-y}Fe_xCr_y(OH)_2$ (b). The light blue, purple, dark blue, red and white balls represent Ni, Fe, Cr, O and H atoms, respectively. The * represents an active site. The Gibbs free-energy data of the four steps for the OER in alkaline environment (pH = 14) on $Ni_{1-x}Fe_x(OH)_2$ (c) and $Ni_{1-x-y}Fe_xCr_y(OH)_2$ (d). (For interpretation of the references to colour in this figure legend, the reader is referred to the web version of this article.)

be attributed to the redistributions of local charge on the surface due to the electronegativity difference between Cr and Fe, it is thus revealed intuitively that the electrons were accumulated on the Fe as shown in Fig. 1(e-f). Consequently, it is favourable to escalate the catalytic process, as already well documented that the Fe species served as the active sites in $Ni_{1-x}Fe_x(OH)_2$ for water oxidation. The work functions of the $Ni_{1-x}Fe_x(OH)_2$ and $Ni_{1-x-y}Fe_xCr_y(OH)_2$ surfaces were 5.13 eV and 4.09 eV, respectively, which suggested that the electrons in the latter were more active than those in the former, as shown in Fig. 1(g-h). In addition, energy band (EB) and total density of state (TDOS) were calculated as shown in Fig. 1(i-k) to estimate the conductivity of the two catalysts. Compared with pristine $Ni_{1-x}Fe_x(OH)_2$, in the neighbouring Fermi level, substantial new EB emerged which was caused by the intense electron interactions between Cr and Fe. For these two TDOS curves, the magnetic property is confirmed by the asymmetrical splitting of the spin-up and spin-down channels. The enhanced electronic conductivity after Cr-doping was derived from the appearance of spin-up states near the Fermi level. It gave rise to narrow the band gap to 0.52 eV between the valence band (VB) and the conducting band (CB) of $Ni_{1-x-y}Fe_xCr_y(OH)_2$. A further understanding of electronic structures was gleaned from the projected density of states (PDOS) of active site and doping site (Fig. S1 and Fig. S2). The noticeable impact on the TDOS of $Ni_{1-x-y}Fe_xCr_y(OH)_2$ came from the 3d-ortitals of Fe and Cr, rather than the extremely weak s or p states. Ranging from 0 to 2.5 eV near the Fermi level, two sharp spin-up states appeared of Cr-3d orbital manifest that the optimization of electrical conductivity could be attributed to the polarized electrons. Moreover, the electron of Fe-3d orbital was no longer occupying a lower energy level (-10 ~ -5 eV), while moving in the direction of the Fermi level (-5 eV ~ 0 eV), after substituted by Cr in the lattice of $Ni_{1-x}Fe_x(OH)_2$. This result indicated that a certain electronic influence and coupling was produced between the Fe-3d and Cr-3d orbitals. According to the d-band theory, the positive movement of d orbital centers of the active site would strengthen the adsorption, thus leading to high catalytic activity. Therefore, Cr doping facilitated charge transfer and excellent electron conductivity, which is imperative cornerstone for electrochemical reaction.

Due to the relationship between electronic structure and activity, the pathways of complete OER reaction circle were mapped out to further investigate the impact of Cr doping from thermodynamic view as shown in Fig. 2. For a long time, it has been a complicated issue of controversy to determine whether Ni or Fe was the main contributing factor for its unmatched catalytic performance [42]. Whereas the evidences towards the view that Fe sites were acting as the active centers have been increasingly supported by the experimental and computational consequences, which are attributed to the powerful and advanced observation technologies [43,44,45,46,47,48]. Therefore, the Fe atom also regarded as the origin of catalytic activity in our model catalysts, as can be observed from Fig. 2(a-b). It was opted as the reactive center to adsorb the intermediates in simulating the OER process according to the classic $4e^-$ mechanism proposed by Nørskov [49]. Based on that, it contains four elementary processes because one electron transfer at a time was energetically more favourable than transfer of more than one electron. For the alkaline system (pH = 14), we simulated the Gibbs energy under different electrode potentials $U = 0$ V and $U = 0.402$ V (equilibrium potential) to determine the rate-limiting step as shown in Fig. 2(c-d) and Table S3. For $Ni_{1-x}Fe_x(OH)_2$, since the reaction sub-step (4) is downhill, the other sub-reactions (1), (2) and (3) are all uphill. The rate-limiting step is the adsorption of H_2O to form OH*, the maximum uphill, and the overpotential for the OER is 1.07 V. On the contrary, the reaction rate-limiting step of $Ni_{1-x-y}Fe_xCr_y(OH)_2$ as shown in red line of Fig. 2(d) is changed to the desorption of the O* to form OOH*, in which the overpotential is determined to be 0.86 V. These results indicate that the doped Cr regulates the bonding strength between $Ni_{1-x-y}Fe_xCr_y(OH)_2$ and OER intermediates (O*, OH* and OOH*), to have an optimum one that is not too strong or too weak, in consistent with Sabatier principle.

Inspired by these theoretical results, we synthesized the $Ni_{0.66}Fe_{0.27}Cr_{0.07}(OH)_2$/NF array to verify the above prediction. The synthesis process and the microstructure of $Ni_{0.66}Fe_{0.27}Cr_{0.07}(OH)_2$/NF are shown in Fig. 3(a). Via a one-step hydrothermal method, the vertically aligned $Ni_{0.66}Fe_{0.27}Cr_{0.07}(OH)_2$/NF nanosheets by using nitrates of transition metals and urea as the precursors and precipitant. As Cr^{3+} substituted partial Fe^{3+}, the colour of $Ni_{0.66}Fe_{0.27}Cr_{0.07}(OH)_2$/NF was lighter than that of $Ni_{0.66}Fe_{0.34}(OH)_2$ (Fig. S3). Fig. 3(b-c) show the SEM images of $Ni_{0.66}Fe_{0.27}Cr_{0.07}(OH)_2$/NF, in which the vertically aligned nanosheets were uniformly grown on the Ni foam substrate.

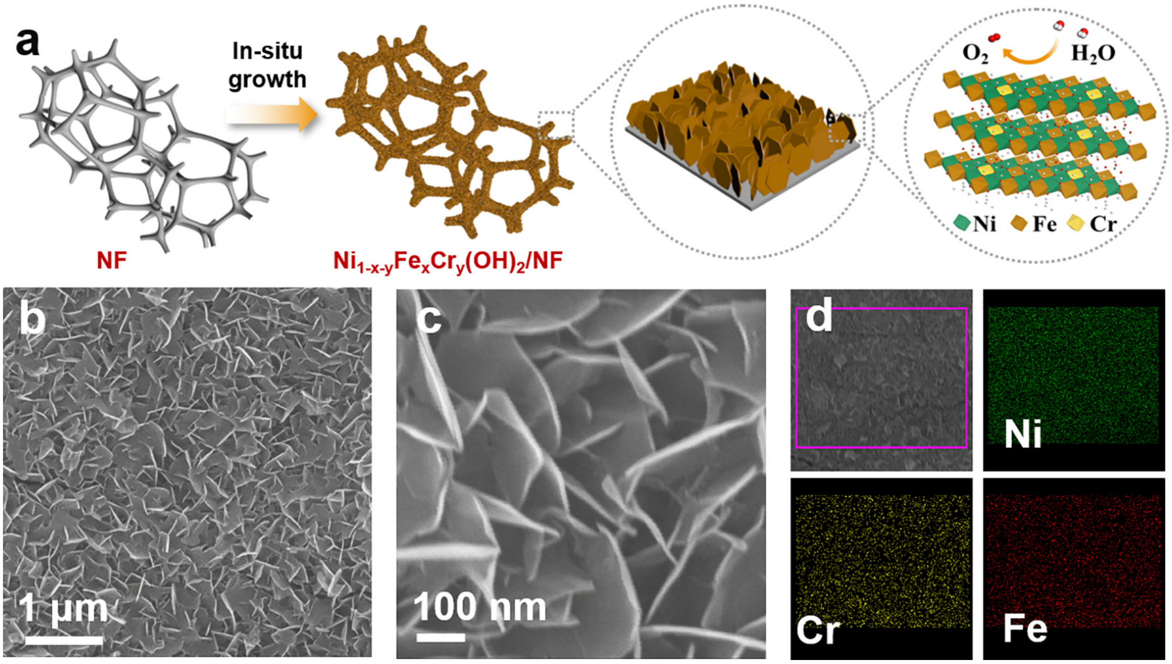

Fig. 3. (a) Schematic illustration of the $Ni_{1-x-y}Fe_xCr_y(OH)_2$/NF nanosheet arrays prepared via a one-step hydrothermal method; (b) low and (c) high magnification SEM images of $Ni_{0.66}Fe_{0.27}Cr_{0.07}(OH)_2$/NF nanosheet arrays; (d) the elemental mapping images of $Ni_{0.66}Fe_{0.27}Cr_{0.07}(OH)_2$/NF.

The morphology of $Ni_{0.66}Fe_{0.27}Cr_{0.07}(OH)_2$/NF is similar to that of $Ni_{0.66}Fe_{0.34}(OH)_2$/NF (Fig. S4), indicating that the morphology was maintained after doping of Cr. The EDS elemental mapping images in Fig. 3(d) indicate that the doping was uniform and homogeneous without any aggregation. A high magnification SEM image in Fig. S4 reveals that 3D architecture was well oriented and porous, which was beneficial to increase the active surface area. The ultra-thin structure of the $Ni_{0.66}Fe_{0.27}Cr_{0.07}(OH)_2$/NF, merely 6–7 octahedral atomic layers, was observed by the TEM images in Fig. S5. The selected area electron diffraction (SAED) pattern (Fig. S4) exhibits the six-fold point pattern. These results confirmed the hexagonal crystal phase of the $Ni_{0.66}Fe_{0.27}Cr_{0.07}(OH)_2$/NF and the diffraction rings indexed of the (1 0 1), (0 1 5), and (1 1 0) lattices as observed in XRD pattern (Fig. S6, red line), which was accordant with the XRD. In Fig. 3F, six peaks located at 11.4°, 22.9°, 33.5°, 34.4°, 59.9° and 61.1° can be identified, corresponding to (0 0 3), (0 0 6), (1 0 1), (0 1 2), (1 1 0) and (1 1 6) diffraction peaks, respectively. In addition, peaks marked by "#" can be well indexed to Ni foam substrate (JCPDF 04–0850). For this type of martials, what still needed to be explained is that the weak miscellaneous signals were incurred by the limited signal-to-noise ratio, which were attributed to the stronger peaks of Ni foam substrate, the rough material surface, and the limited active substance loading [50]. Through the careful analysis of the above data, it is evidenced that Cr was not only easy to get into but also non-destructive to the structure of parental $Ni_{0.66}Fe_{0.34}(OH)_2$/NF, which agrees well with the computational insights.

In order to further verify and understand the theoretical data of electronic structure, the XPS was used to characterize the surface chemical composition and oxidation state of metal cations in $Ni_{0.66}Fe_{0.27}Cr_{0.07}(OH)_2$/NF and $Ni_{0.66}Fe_{0.34}(OH)_2$/NF as shown in Fig. 4. The coexistence of Ni, Fe, Cr, O and C elements in $Ni_{0.66}Fe_{0.27}Cr_{0.07}(OH)_2$ was evidenced by the signals in the profile surveys (Fig. 4(a), red line), which were consistent with EDS elemental mapping results in Fig. 3(d). What needs illustration is that the weak valence change of Ni could not be detected, which is limited by the accuracy of XPS. Hence, for $Ni_{0.66}Fe_{0.27}Cr_{0.07}(OH)_2$/NF and $Ni_{0.66}Fe_{0.34}(OH)_2$/NF in Fig. 4(b), their Ni 2p3/2 and 2p1/2 (resulting from the spin–orbit splitting) spectra were situated at the same location without shifting, which is identical to the theoretical prediction in Fig. 1e-f [51,52,53]. When it came to Fe 2p XPS in Fig. 4(c), two fitting peaks at 713.0 eV and 715.8 eV were observed and assigned to 2p3/2 and 2p1/2, respectively [54,55]. It is interesting to note that, Fe 2p peaks shifted negatively about 0.49 eV after chromium doping, which was marked by two reversed arrows. The decreased binding energy of Fe confirmed that the chemical environment of Fe (III) was modified due to the Cr doping and the electron transfer between Fe and doped Cr, which was in accordance to the theoretical results in Fig. 1. The Cr 2p spectrum was also splitting into 2p3/2 and 2p1/2 with a difference of ~0.9 eV. As for Cr 2p3/2 spectrum in Fig. 4(d), three components could be distinguished at 577.4 eV (pink), 576.5 eV (blue) and 578.4 eV (purple), which were in good agreement with three-, four-, and five-valence state, respectively [56,57,58]. The shifting peak of Fe 2p was generated by the electronic coupling and transfer between Cr and Fe. Some electrons transferred from the electron-rich Cr to the electron-acceptive Fe via Cr-O-Fe bonds, which incurred the bonding energy of the Fe 2p increased. Initial Cr (III), the major contributor to electronic coupling, translated into Cr (IV) and Cr(V) after the charge transfer. Besides, Cr^{3+} may also be partially oxidized to higher oxidation sates

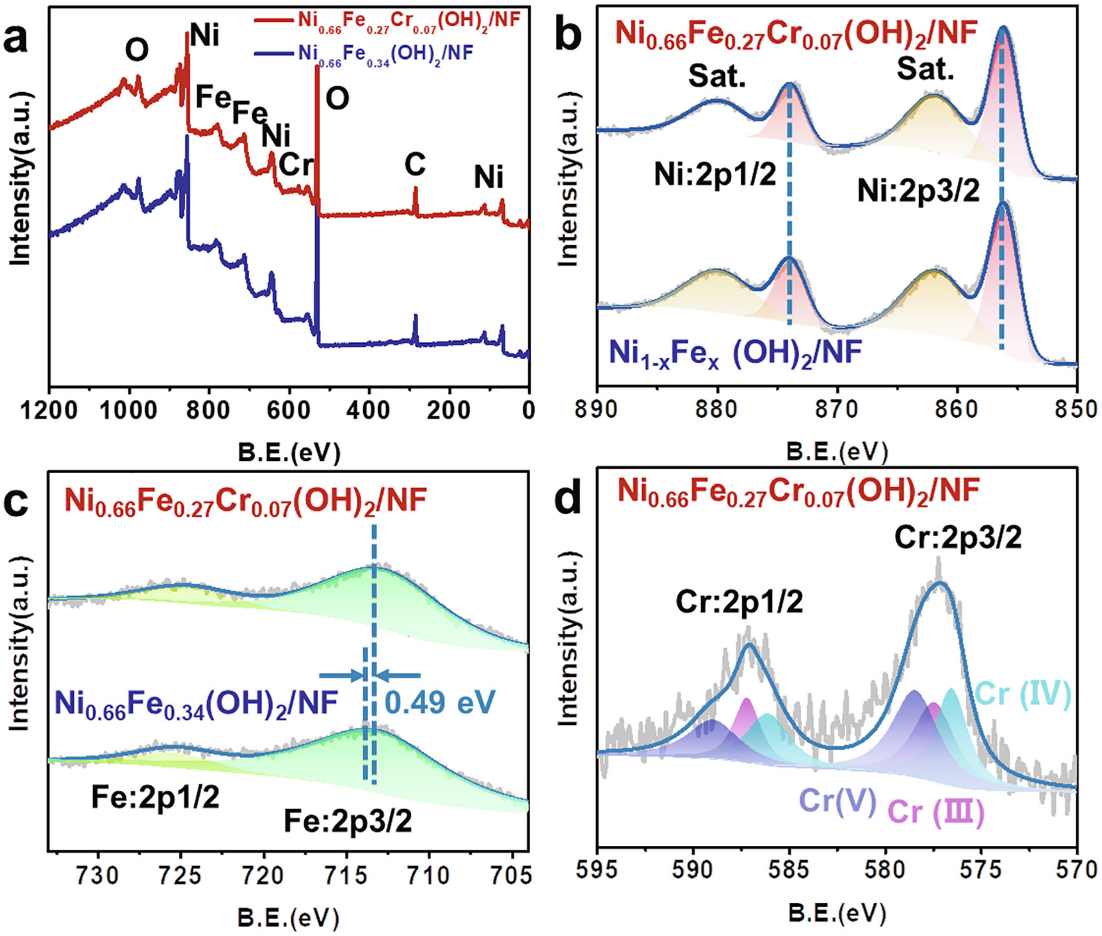

Fig. 4. (a) X-ray photoelectron spectroscopy (XPS) survey spectra of $Ni_{0.66}Fe_{0.27}Cr_{0.07}(OH)_2$/NF and $Ni_{0.66}Fe_{0.34}(OH)_2$/NF; (b-d) high-resolution XPS spectra for (b) Ni 2p region, (c) Fe 2p region and (d) Cr 2p region, with peak fitting analysis of $Ni_{0.66}Fe_{0.27}Cr_{0.07}(OH)_2$/NF and $Ni_{0.66}Fe_{0.34}(OH)_2$/NF.

by oxygen during the synthesis [59].This result confirmed that the electronic interaction exists between foreign chromium and parental iron as discussed in the above calculation part.

Then the electrocatalytic activities of $Ni_{0.66}Fe_{0.27}Cr_{0.07}(OH)_2$/NF catalysts towards oxygen evolution reaction were systematically studied. The linear sweep voltammetry (LSV) polarization curves of OER were obtained as shown in Fig. 5(a) at a slow scan rate of 1 mV s^{-1}. The $Ni_{0.66}Fe_{0.27}Cr_{0.07}(OH)_2$/NF displayed the earliest onset potential and the fastest current density increase, which exhibited a more remarkable catalytic activity than the commercial RuO_2/NF. The TOF of three catalysts at overpotential of 300 mV was listed in the Table S5. The $Ni_{0.66}Fe_{0.27}Cr_{0.07}(OH)_2$/NF showcased a higher TOF of 0.032 s^{-1} than that of pristine $Ni_{0.66}Fe_{0.34}(OH)_2$/NF (0.019 s^{-1}) and $Ni_{0.66}Cr_{0.34}(OH)_2$/NF (0.001 s^{-1}), demonstrating its much enhanced intrinsic electrocatalytic activity for OER. A series of Cr/Fe ratios (0/10, 1/9, 2/8, 5/5, 8/2, 10/0) were applied to further explore the influence of the Cr content (Fig. S7). There is a "volcanic" relationship between the Cr/Fe content and OER catalytic activity. Specifically speaking, when the Cr concentration was too high, the catalyst component gradually turned into a less active $Ni_{1-x}Cr_x(OH)_2$/NF. By contrast, if it was too low, the influence of tuning electronic coupling would be weakened. Only when the Cr/Fe content (8/2) was at some appropriate value would the performance be at the peak of the "volcano". The result also indicated that the co-existence of both Fe and Cr is vital to enhance the OER property by coupling effects, they acted as active centers and regulators, respectively. In the LSV curve, a modest peak at ~ 1.42 V emerged on account of Ni^{2+}/Ni^{3+} oxidation reaction. In order to exclude the effect of above side reaction, we identified the onset potential and overpotential by virtue of the reverse scan of stable cyclic voltammetry (CV) curve (the 20th segment) from positive to negative potential (Fig. S8). At a current density of 10 mA cm^{-2}, the optimized $Ni_{0.66}Fe_{0.27}Cr_{0.07}(OH)_2$/NF (Fig. S5) showed an overpotential of only 231 mV, which was lower than that of $Ni_{0.66}Fe_{0.34}(OH)_2$/NF (241 mV). Furthermore, the $Ni_{0.66}Fe_{0.27}Cr_{0.07}(OH)_2$/NF achieved a high current density of 20 mA cm^{-2} at an overpotential of 235 mV. In contrast, $Ni_{0.66}Fe_{0.34}(OH)_2$/NF required an overpotential of 246 mV to obtain the same current density. The superior OER activity of the $Ni_{0.66}Fe_{0.27}Cr_{0.07}(OH)_2$/NF electrode was further confirmed by its small Tafel slope of ~ 31 mV dec^{-1} as shown in Fig. 5(b), which was much lower than that of $Ni_{0.66}Fe_{0.34}(OH)_2$/NF (~55 mV dec^{-1}) and $Ni_{0.66}Cr_{0.34}(OH)_2$/NF (~86 mV dec^{-1}). Then, we investigated the band gap of valence band and conduction band by diffuse reflectance UV–visible (UV–vis) spectroscopy. The intersection of tangent and abscissa in Fig. S9 revealed a smaller band gap of $Ni_{0.66}Fe_{0.27}Cr_{0.07}(OH)_2$ compared with that of $Ni_{0.66}Fe_{0.34}(OH)_2$/NF, agreeing well with the DFT + U computations in Fig. 1(k) and colour evolution as shown in Fig. S3. The unidentical data from theoretical prediction to experimental validation was caused by the simplified models employed rationally, which utilizing the regular monolayer array to replace the uncertain and complicated orientations. But this did not alter our judgment about the relative trends of the band gap between $Ni_{1-x-y}Fe_xCr_y(OH)_2$ and $Ni_{1-x}Fe_x(OH)_2$. Furthermore, the electrochemical impedance spectroscopy (EIS) measurements were conducted to evaluate the kinetics of charge transfer (Fig. S10). In addition, The EIS results can be transformed into the equivalent circuit model (Fig. S11), composed an ohmic resistor (R_e) in series with a parallel combination of a resistor (R_{ct}) and a constant phase element (CPE) as the previous works [60,61]. R_e comes mainly from the resistance of the electrolyte, the electrocatalysts and all the contacts. The charge transfer resistance R_{ct} values represent the kinetics rate for OER process. The $Ni_{0.66}Fe_{0.27}Cr_{0.07}(OH)_2$/NF shows a lower R_{ct} (0.55 Ω) than $Ni_{0.66}Fe_{0.34}(OH)_2$/NF (0.92 Ω), indicating that the former had a faster charge-transfer rate (Table. S6). Based on above results, we concluded that the enhancement of OER activity of $Ni_{0.66}Fe_{0.27}Cr_{0.07}(OH)_2$/NF is

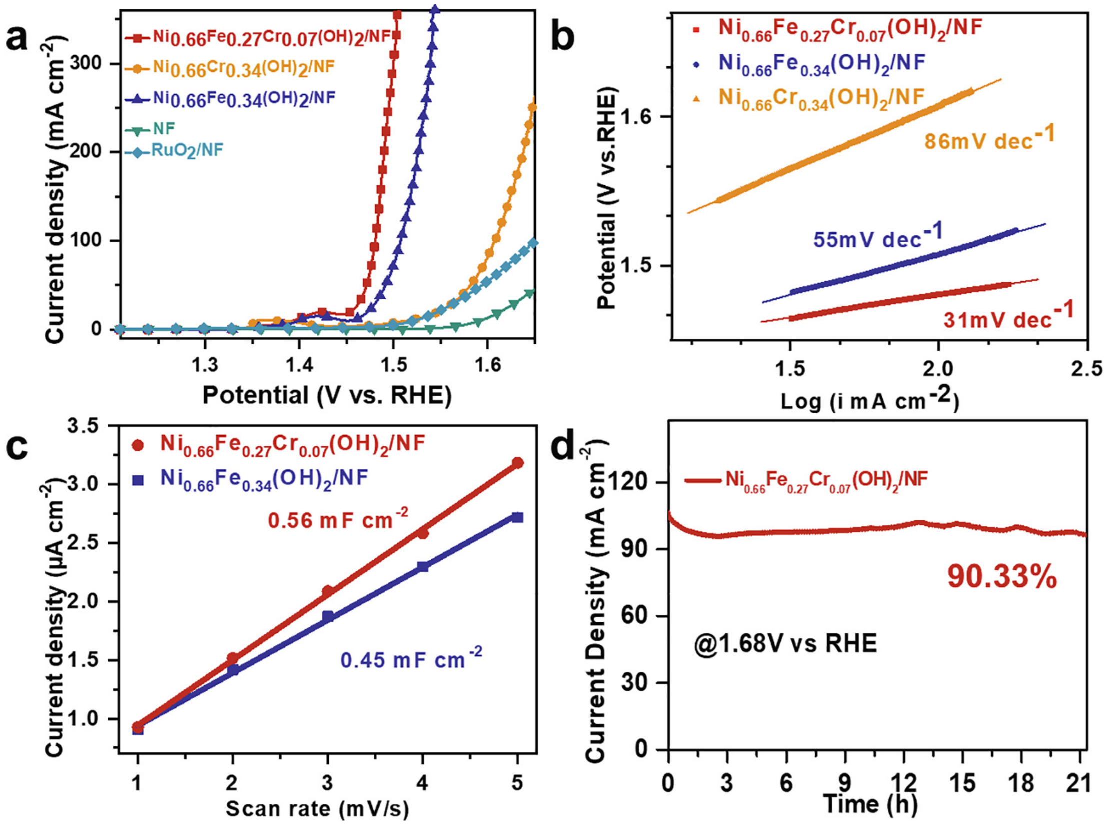

Fig. 5. (a) Polarization curves of $Ni_{0.66}Fe_{0.27}Cr_{0.07}(OH)_2$/NF, $Ni_{0.66}Fe_{0.34}(OH)_2$/NF, $Ni_{0.66}Cr_{0.34}(OH)_2$/NF, NF and RuO_2/NF at a scan rate of 1 mV s^{-1}. (b) The corresponding Tafel plots of $Ni_{0.66}Fe_{0.27}Cr_{0.07}(OH)_2$/NF, $Ni_{0.66}Fe_{0.34}(OH)_2$/NF and $Ni_{0.66}Cr_{0.34}(OH)_2$/NF. (c) The double-layer capacity (C_{dl}) calculations for $Ni_{0.66}Fe_{0.27}Cr_{0.07}(OH)_2$/NF and $Ni_{0.66}Fe_{0.34}(OH)_2$/NF. (d) The stability test of $Ni_{0.66}Fe_{0.27}Cr_{0.07}(OH)_2$/NF for the OER at a fixed potential of 1.68 V vs RHE.

attributed to the modulated electronic structure of active sites and higher electron transfer ability due to Cr embedding. In addition, Fig. 5(c) (obtained from data in Fig. S12) demonstrated that $Ni_{0.66}Fe_{0.27}Cr_{0.07}(OH)_2$/NF possessed a much higher electrochemical active surface area (ECSA)/C_{dl} than that of $Ni_{0.66}Fe_{0.34}(OH)_2$/NF, leading to a faster increase in OER current density. For a reasonable comparison, we normalized the current densities of $Ni_{0.66}Fe_{0.27}Cr_{0.07}(OH)_2$/NF and $Ni_{0.66}Fe_{0.34}(OH)_2$/NF to their corresponding ECSA. Fig. S13 apparently showcased that the former had a high intrinsic activity than the latter. By comparison with the other similar martials as summarized in the Table S7, the as-predicted and prepared $Ni_{0.66}Fe_{0.27}Cr_{0.07}(OH)_2$/NF showed certain superiority and competitiveness. Furthermore, a high stability of the over 90% current density was obtained for 21 h at a fixed potential of 1.68 V vs RHE as shown in Fig. 5(d), revealing the remarkable durability of the electrode for OER at a highly oxidative potential. The almost identical CV curves of the initial and 1000th circles indicated that the composition of $Ni_{0.66}Fe_{0.27}Cr_{0.07}(OH)_2$/NF catalyst had maintained without noticeable change (Fig. S14). The $Ni_{0.66}Fe_{0.27}Cr_{0.07}(OH)_2$/NF kept the initial elements and nanosheet morphology without significant variation after scanning 1000 CVs (Fig. S13). The XPS results manifested that Cr composition held in the trimetallic system after OER testing (Fig. S14). Since the XPS was not collected in situ, the further oxidation of the samples might occur before XPS test, which caused a change in the valence state [28]. Although some works suggested that Cr was leached in amorphous oxide/(oxy)hydroxide catalysts [27], it seems that mixing Cr ions into two vertically arrayed nanosheets could form a stable trimetallic system and facilitate the OER process. The substantial presence of Cr confirmed that the improvement of OER activity was greatly contributed to the electronic interplay between Cr and Fe as shown in the above theoretical prediction and experimental validation.

4. Conclusions

In summary, we have demonstrated the importance of tuning electronic structures for the rational design of advanced catalysts, with ternary $Ni_{1\text{-}x\text{-}y}Fe_xCr_y$ based hydroxides as model systems. Based on the theoretical prediction, $Ni_{0.66}Fe_{0.27}Cr_{0.07}(OH)_2$/NF nanosheet arrays were prepared by a simple hydrothermal method and served as a highly active and stable anode catalyst for water splitting. Among all nanosheet arrays with different molar ratios of the three metal cations, $Ni_{0.66}Fe_{0.27}Cr_{0.07}(OH)_2$/NF was identified as an optimal one which exhibited a superior activity and a high stability towards OER, i.e., with a small overpotential of 231 mV to achieve a significant current density of 10 mA cm^{-2}, a low Tafel slope of 31 mV dec^{-1} and a satisfying stability at a highly oxidative potential of 1.68 V vs RHE. The DFT + U calculation and the experiment analysis jointly confirm that the outstanding catalytic performance comes from the synergistic effect between the parental Fe and foreign Cr elements, in which Cr doping promotes the electron transfer to accelerate the kinetics of OER as well as exposes more electrochemical active sites.

Declaration of Competing Interest

The authors declare that they have no known competing financial interests or personal relationships that could have appeared to influence the work reported in this paper.

Acknowledgements

This study was financially supported by the National Key Research and Development Project (2018YFB1502401, 2018YFA0702002 and 2017YFA0206500), the National Natural Science Foundation of China (51732002), the Program for Changjiang Scholars and Innovative Research Team in the University (IRT1205), the U.S. National Science Foundation (16662288), the Royal Society and the Newton Fund through the Newton Advanced Fellowship award (NAF\R1\191294). The authors thank the Sino-Foreign Cooperative Training Project of BUCT.

Appendix A. Supplementary data

Supplementary data to this article can be found online at https://doi.org/10.1016/j.cej.2020.126144.

References

[1] J.A. Turner, Sustainable Hydrogen Production, Science 305 (2004) 972–974.

[2] A. Thakur, D. Ghosh, P. Devi, K.-H. Kim, P. Kumar, Current progress and challenges in photoelectrode materials for the production of hydrogen, Chem. Eng. J. 397 (2020) 125415.

[3] I. Roger, M.A. Shipman, M.D. Symes, Earth-abundant catalysts for electrochemical and photoelectrochemical water splitting, Nat. Rev. Chem. 1 (2017) 0003.

[4] X.X. Zou, Y. Zhang, Noble metal-free hydrogen evolution catalysts for water splitting, Chem. Soc. Rev. 44 (2015) 5148–5180.

[5] P.T. Babar, A.C. Lokhande, M.G. Gang, B.S. Pawar, S.M. Pawar, J.H. Kim, Thermally oxidized porous NiO as an efficient oxygen evolution reaction (OER) electrocatalyst for electrochemical water splitting application, J. Ind. Eng. Chem. 60 (2018) 493–497.

[6] N.-T. Suen, S.-F. Hung, Q. Quan, N. Zhang, Y.-J. Xu, H.M. Chen, Electrocatalysis for the oxygen evolution reaction: recent development and future perspectives, Chem. Soc. Rev. 46 (2017) 337–365.

[7] D.A. Kuznetsov, B. Han, Y. Yu, R.R. Rao, J. Hwang, Y. Román-Leshkov, Y. Shao-Horn, Tuning Redox Transitions via Inductive Effect in Metal Oxides and Complexes, and Implications in Oxygen Electrocatalysis, Joule 2 (2018) 225–244.

[8] Y.Y. Wang, D.F. Yan, S. El Hankari, Y.Q. Zou, S.Y. Wang, Recent Progress on Layered Double Hydroxides and Their Derivatives for Electrocatalytic Water Splitting, Adv. Sci. 5 (2018) 1800064.

[9] M.P. Browne, Z. Sofer, M. Pumera, Layered and two dimensional metal oxides for electrochemical energy conversion, Energy Environ. Sci. 12 (2019) 41–58.

[10] L. Lei, D.L. Huang, C.Y. Zhou, S. Chen, X.L. Yan, Z.H. Li, W.J. Wang, Demystifying the active roles of NiFe-based oxides/(oxy)hydroxides for electrochemical water splitting under alkaline conditions, Coord. Chem. Rev. 408 (2020) 213177.

[11] M. Gong, Y.G. Li, H.L. Wang, Y.Y. Liang, J.Z. Wu, J.G. Zhou, J. Wang, T. Regier, F. Wei, H.J. Dai, An Advanced Ni–Fe Layered Double Hydroxide Electrocatalyst for Water Oxidation, J. Am. Chem. Soc. 135 (2013) 8452–8455.

[12] M. Gong, H.J. Dai, A mini review of NiFe-based materials as highly active oxygen evolution reaction electrocatalysts, Nano Res. 8 (2015) 23–39.

[13] Z.Y. Lu, L. Qian, Y. Tian, Y.P. Li, X.M. Sun, X. Duan, Ternary NiFeMn layered double hydroxides as highly-efficient oxygen evolution catalysts, Chem. Commun. 52 (2016) 908–911.

[14] D.J. Zhou, Z. Cai, Y. Jia, X.Y. Xiong, Q.X. Xie, S.Y. Wang, Y. Zhang, W. Liu, H.H. Duan, X.M. Sun, Activating basal plane in NiFe layered double hydroxide by Mn2+ doping for efficient and durable oxygen evolution reaction, Nanoscale Horiz. 3 (2018) 532–537.

[15] A.-L. Wang, H. Xu, G.-R. Li, NiCoFe Layered Triple Hydroxides with Porous Structures as High-Performance Electrocatalysts for Overall Water Splitting, ACS Energy Lett. 1 (2016) 445–453.

[16] X. Long, S. Xiao, Z.L. Wang, X.L. Zheng, S.H. Yang, Co intake mediated formation of ultrathin nanosheets of transition metal LDH—an advanced electrocatalyst for oxygen evolution reaction, Chem. Commun. 51 (2015) 1120–1123.

[17] P.S. Li, X.X. Duan, Y. Kuang, Y.P. Li, G.X. Zhang, W. Liu, X.M. Sun, Tuning Electronic Structure of NiFe Layered Double Hydroxides with Vanadium Doping toward High Efficient Electrocatalytic Water Oxidation, Adv. Energy Mater. 8 (2018) 1703341.

[18] C.S. Lim, C.K. Chua, Z. Sofer, K. Klímová, C. Boothroyd, M. Pumera, Layered transition metal oxyhydroxides as tri-functional electrocatalysts, J. Mater. Chem. A 3 (2015) 11920–11929.

[19] J. Suntivich, K.J. May, H.A. Gasteiger, J.B. Goodenough, Y. Shao-Horn, A Perovskite Oxide Optimized for Oxygen Evolution Catalysis from Molecular Orbital Principles, Science 334 (2011) 1383–1385.

[20] M.A. Hassan, F. Ahmad, Z.M. Abd El-Fattah, Novel identification of ultraviolet/visible Cr6+/Cr3+ optical transitions in borate glasses, J. Alloys Compd. 750 (2018) 320-327.

[21] W. Ye, X.Y. Fang, X.B. Chen, D.P. Yan, A three-dimensional nickel–chromium layered double hydroxide micro/nanosheet array as an efficient and stable bifunctional electrocatalyst for overall water splitting, Nanoscale 10 (2018) 19484–19491.

[22] J.-H. Chen, X.-L. Wang, Z.-Q. Gong, Mechanism and behaviors of Cr3+-doped TiO2, Journal of Central South University of Technology 12 (2005) 59–64.

[23] C.L. Dong, X.T. Yuan, X. Wang, X.Y. Liu, W.J. Dong, R.Q. Wang, Y.H. Duan, F.Q. Huang, Rational design of cobalt–chromium layered double hydroxide as a highly efficient electrocatalyst for water oxidation, J. Mater. Chem. A 4 (2016) 11292–11298.

[24] J.B. Gerken, S.E. Shaner, R.C. Massé, N.J. Porubsky, S.S. Stahl, A survey of diverse earth abundant oxygen evolution electrocatalysts showing enhanced activity from Ni–Fe oxides containing a third metal, Energy Environ. Sci. 7 (2014) 2376–2382.

[25] C. Schwanke, H.S. Stein, L. Xi, K. Sliozberg, W. Schuhmann, A. Ludwig, K.M. Lange, Correlating Oxygen Evolution Catalysts Activity and Electronic Structure by a High-Throughput Investigation of Ni1-y-zFeyCrzOx, Sci. Rep. 7 (2017) 44192.

[26] R.N. Singh, J.P. Singh, B. Lal, M.J.K. Thomas, S. Bera, New NiFe2−xCrxO4 spinel films for O2 evolution in alkaline solutions, Electrochim. Acta 51 (2006) 5515–5523.

[27] D.Y. Xu, M.B. Stevens, Y.C. Rui, G. DeLuca, S.W. Boettcher, E. Reichmanis, Y.G. Li, Q.H. Zhang, H.Z. Wang, The role of Cr doping in NiFe oxide/(oxy)hydroxide electrocatalysts for oxygen evolution, Electrochim. Acta 265 (2018) 10–18.

[28] Y. Yang, L.N. Dang, M.J. Shearer, H.Y. Sheng, W.J. Li, J. Chen, P. Xiao, Y.H. Zhang, R.J. Hamers, S. Jin, Highly Active Trimetallic NiFeCr Layered Double Hydroxide Electrocatalysts for Oxygen Evolution Reaction, Adv. Energy Mater. 8 (2018) 1703189.

[29] L.P. Zhang, C.-Y. Lin, D.T. Zhang, L.L. Gong, Y.H. Zhu, Z.H. Zhao, Q. Xu, H.J. Li, Z.H. Xia, Guiding Principles for Designing Highly Efficient Metal-Free Carbon Catalysts, Adv. Mater. 31 (2019) 1805252.

[30] Z.W. Seh, J. Kibsgaard, C.F. Dickens, I. Chorkendorff, J.K. Nørskov, T.F. Jaramillo, Combining theory and experiment in electrocatalysis: Insights into materials design, Science 355 (2017) eaad4998.

[31] Z.-J. Zhao, S.H. Liu, S.J. Zha, D.F. Cheng, F. Studt, G. Henkelman, J.L. Gong, Theory-guided design of catalytic materials using scaling relationships and reactivity descriptors, Nat. Rev. Mater. 4 (2019) 792–804.

[32] T. Miyake, F. Aryasetiawan, Screened Coulomb interaction in the maximally localized Wannier basis, Phys. Rev. B 77 (2008) 085122.

[33] R.G. Parr, Density Functional Theory of Atoms and Molecules, in: K. Fukui, B. Pullman (Eds.) Horizons of Quantum Chemistry, Springer Netherlands, Dordrecht, 1980, pp. 5-15.

[34] G. Kresse, J. Furthmüller, Efficiency of ab-initio total energy calculations for metals and semiconductors using a plane-wave basis set, Comput. Mater. Sci. 6 (1996) 15–50.

[35] J.P. Perdew, K. Burke, M. Ernzerhof, Generalized Gradient Approximation Made Simple, Phys. Rev. Lett. 77 (1996) 3865–3868.

[36] B. Hammer, L.B. Hansen, J.K. Nørskov, Improved adsorption energetics within density-functional theory using revised Perdew-Burke-Ernzerhof functionals, Phys. Rev. B 59 (1999) 7413–7421.

[37] S.L. Dudarev, G.A. Botton, S.Y. Savrasov, Z. Szotek, W.M. Temmerman, A.P. Sutton, Electronic Structure and Elastic Properties of Strongly Correlated Metal Oxides from First Principles: LSDA + U, SIC-LSDA and EELS Study of UO2 and NiO, Physica Status Solidi (a) 166 (1998) 429–443.

[38] H.X. Xu, D.J. Cheng, D.P. Cao, X.C. Zeng, A universal principle for a rational design of single-atom electrocatalysts, Nat. Catal. 1 (2018) 339–348.

[39] C.-Y. Lin, L.P. Zhang, Z.H. Zhao, Z.H. Xia, Design Principles for Covalent Organic Frameworks as Efficient Electrocatalysts in Clean Energy Conversion and Green Oxidizer Production, Adv. Mater. 29 (2017) 1606635.

[40] L.L. Gong, D.T. Zhang, C.-Y. Lin, Y.H. Zhu, Y. Shen, J. Zhang, X. Han, L.P. Zhang, Z.H. Xia, Catalytic Mechanisms and Design Principles for Single-Atom Catalysts in Highly Efficient CO2 Conversion, Adv. Energy Mater. 9 (2019) 1902625.

[41] I.V. Solovyev, P.H. Dederichs, V.I. Anisimov, Corrected atomic limit in the local-density approximation and the electronic structure of d impurities in Rb, Phys. Rev. B 50 (1994) 16861–16871.

[42] C.L. Peng, N. Ran, G. Wan, W.P. Zhao, Z.Y. Kuang, Z. Lu, C.J. Sun, J.J. Liu, L.Z. Wang, H.R. Chen, Engineering Active Fe Sites on Nickel-Iron Layered Double Hydroxide through Component Segregation for Oxygen Evolution Reaction, ChemSusChem 13 (2020) 811–818.

[43] L. Trotochaud, S.L. Young, J.K. Ranney, S.W. Boettcher, Nickel-Iron Oxyhydroxide Oxygen-Evolution Electrocatalysts: The Role of Intentional and Incidental Iron Incorporation, J. Am. Chem. Soc. 136 (2014) 6744–6753.

[44] D. Friebel, M.W. Louie, M. Bajdich, K.E. Sanwald, Y. Cai, A.M. Wise, M.-J. Cheng, D. Sokaras, T.-C. Weng, R. Alonso-Mori, R.C. Davis, J.R. Bargar, J.K. Nørskov, A. Nilsson, A.T. Bell, Identification of Highly Active Fe Sites in (Ni, Fe)OOH for Electrocatalytic Water Splitting, J. Am. Chem. Soc. 137 (2015) 1305–1313.

[45] J.Y.C. Chen, L. Dang, H. Liang, W. Bi, J.B. Gerken, S. Jin, E.E. Alp, S.S. Stahl, Operando Analysis of NiFe and Fe Oxyhydroxide Electrocatalysts for Water Oxidation: Detection of Fe4+ by Mössbauer Spectroscopy, J. Am. Chem. Soc. 137 (2015) 15090–15093.

[46] S. Klaus, Y. Cai, M.W. Louie, L. Trotochaud, A.T. Bell, Effects of Fe Electrolyte Impurities on Ni(OH)2/NiOOH Structure and Oxygen Evolution Activity, The Journal of Physical Chemistry C 119 (2015) 7243–7254.

[47] Z.K. Goldsmith, A.K. Harshan, J.B. Gerken, M. Vörös, G. Galli, S.S. Stahl, S. Hammes-Schiffer, Characterization of NiFe oxyhydroxide electrocatalysts by integrated electronic structure calculations and spectroelectrochemistry, Proc. Natl. Acad. Sci. 114 (2017) 3050.

[48] B.M. Hunter, N.B. Thompson, A.M. Müller, G.R. Rossman, M.G. Hill, J.R. Winkler, H.B. Gray, Trapping an Iron(VI) Water-Splitting Intermediate in Nonaqueous Media, Joule 2 (2018) 747–763.

[49] M. García-Mota, A. Vojvodic, H. Metiu, I.C. Man, H.-Y. Su, J. Rossmeisl, J.K. Nørskov, Tailoring the Activity for Oxygen Evolution Electrocatalysis on Rutile TiO2(110) by Transition-Metal Substitution, ChemCatChem 3 (2011) 1607–1611.

[50] T. Li, R. Li, H. Luo, Facile in situ growth of Ni/Co-LDH arrays by hypothermal chemical coprecipitation for all-solid-state asymmetric supercapacitors, J. Mater. Chem. A 4 (2016) 18922–18930.

[51] X. Luo, M. Huang, D. He, M. Wang, Y. Zhang, P. Jiang, Porous NiCo2O4 nanoarray-integrated binder-free 3D open electrode offers a highly efficient sensing platform for enzyme-free glucose detection, Analyst 143 (2018) 2546–2554.

[52] J.H. Lin, X.H. Zheng, Y.H. Wang, H.Y. Liang, H.N. Jia, S.L. Chen, J.L. Qi, J. Cao, W.D. Fei, J.C. Feng, Rational construction of core–shell Ni3S2@Ni(OH)2 nanostructures as battery-like electrodes for supercapacitors, Inorg. Chem. Front. 5 (2018) 1985–1991.

[53] W.B. Fu, Y.L. Wang, W.H. Han, Z.M. Zhang, H.M. Zha, E.Q. Xie, Construction of hierarchical ZnCo2O4@NixCo2x(OH)6x core/shell nanowire arrays for high-performance supercapacitors, J. Mater. Chem. A 4 (2016) 173–182.

[54] J.G. He, Y.L. Shi, X.Y. Yang, W.Q. Zhou, Y. Li, C.L. Liu, Influence of Fe(II) on the Se (IV) sorption under oxic/anoxic conditions using bentonite, Chemosphere 193 (2018) 376–384.

[55] X.H. Hu, J.Y. Xu, M.S. Wu, J.X. Xing, W.S. Bi, K. Wang, J.F. Ma, X.e. Liu, Effects of biomass pre-pyrolysis and pyrolysis temperature on magnetic biochar properties, J. Anal. Appl. Pyrolysis 127 (2017) 196-202.

[56] S. Survilienė, A. Češūnienė, V. Jasulaitienė, I. Jurevičiūtė, The use of XPS for study of the surface layers of CrNi alloys electrodeposited from the Cr(III) + Ni(II) bath, Appl. Surf. Sci. 258 (2012) 9902–9906.

[57] A.I. Karayan, E. Maya-Visuet, H. Castaneda, Transpassive Behavior of UNS N08367 Super Austenitic Stainless Steel in LiBr Solution, Corrosion 71 (2015) 1110–1120.

[58] Y.Y. Yue, C.J. Liu, P.Y. Shi, M.F. Jiang, Passivity of stainless steel in sulphuric acid under chemical oxidation, Corros. Eng., Sci. Technol. 53 (2018) 173–182.

[59] K. Fan, H. Chen, Y.F. Ji, H. Huang, P.M. Claesson, Q. Daniel, B. Philippe, H. Rensmo, F. Li, Y. Luo, L.C. Sun, Nickel–vanadium monolayer double hydroxide for efficient electrochemical water oxidation, Nat. Commun. 7 (2016) 11981.

[60] H.J. Zhang, X.P. Li, A. Hähnel, V. Naumann, C. Lin, S. Azimi, S.L. Schweizer, A.W. Maijenburg, R.B. Wehrspohn, Bifunctional Heterostructure Assembly of NiFe LDH Nanosheets on NiCoP Nanowires for Highly Efficient and Stable Overall Water Splitting, Adv. Funct. Mater. 28 (2018) 1706847.

[61] Y.Y. Wu, G.-D. Li, Y.P. Liu, L. Yang, X.R. Lian, T. Asefa, X.X. Zou, Overall Water Splitting Catalyzed Efficiently by an Ultrathin Nanosheet-Built, Hollow Ni3S2-Based Electrocatalyst, Adv. Funct. Mater. 26 (2016) 4839–4847.